Solvothermal synthesis and electrochemical charge storage assessment of Mn₃N₂

S. Imran U. Shah, Andrew L. Hector,* Xianji Li and John R. Owen

Chemistry, University of Southampton, Highfield, Southampton SO17 1BJ, UK.
A.L.Hector@soton.ac.uk

η-Mn₃N₂ is produced using solvothermal reactions between MnCl₂ and LiNH₂ in benzene. At 350 °C nanocapsule structures are obtained, whereas at higher temperatures samples consisted of isotropic nanoparticulates. In aqueous KOH solution capacitances of up to 300 F g^{-1} (2 mV s^{-1}, potential window 0.3 to -0.6 V vs Hg/HgO), but capacitance fell to relatively low values on cycling. In lithium cells a reversible first cycle capacity of 600 mA h g^{-1} was obtained, and this decayed to 340 mA h g^{-1} after 50 cycles. In sodium cells a reversible first cycle capacity of 156 mA h g^{-1} was obtained and was maintained well on cycling (127 mA h g^{-1} in the 50th cycle).

Introduction

Four major phases exist in the Mn-N binary system. ε-Mn₄N[1] is an anti-perovskite consisting of face centred cubic manganese atoms with nitrogen in ¼ of the octahedral holes. The defect NiAs-type ζ-Mn₂N phase has a range of nitrogen contents typically from MnN$_{0.42}$[2] to Mn₂N$_{1.08}$.[3] with nitrogen occupancy varying according to the composition. η-Mn₃N₂[4,5] and the θ-phases MnN[6] and Mn₆N₅[7] are tetragonally distorted rocksalt-type structures with nitrogen vacancies. Much of the previous interest in manganese nitrides has focussed on their magnetic properties – MnN, Mn₃N₂ and Mn₂N are antiferromagnetic, while Mn₄N is ferromagnetic.[6,8]

Metal nitrides are a current research focus as electrode materials for electrochemical capacitors due to a number of studies that have shown useful capacities on TiN, VN and MoN.[9,10,11,12] The current redox capacitor material of choice is RuO₂, which can deliver capacities of around 720 F g^{-1} but is too costly and toxic for widespread use.[13] A number of other oxides have also been used, but the current interest in nitrides comes from the possibility of producing materials with a high electronic conductivity nitride core and an oxide coating with a high surface area. Manganese dioxide is one promising replacement for RuO₂. It undergoes pseudocapacitive reactions during surface adsorption and intercalation into the bulk of the electrode:[14]

$$MnO_2 + Cat^+ + e^- \leftrightarrow CatMnO_2$$
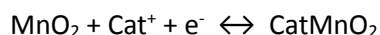
Where Cat⁺ is the electrolyte cation (e.g. H⁺ under aqueous conditions or Li⁺ with an organic electrolyte) and the manganese cycles between the +3 and +4 oxidation states. MnO₂ can deliver capacitances of ~240 F g^{-1}, although this is over a relatively narrow potential range and is subject to some fading during cycling.[15] An oxide surface can develop during cycling of metal nitride electrodes[11] and this prompted our interest in making nanoparticulate manganese nitrides.

There is also a developing literature in the use of metal nitrides as conversion electrodes[16] in lithium and sodium batteries, where the metal nitride is reduced to metal and lithium nitride. In lithium cells capacities during cycling as high as ~1200 mA h g^{-1} have been observed (with CrN[17]), and useful capacity has been observed with Mn_4N,[18] Fe_3N,[19] CoN,[20] Co_3N,[19] Ni_3N[21] and Cu_3N.[22] We have recently reported the use of Ni_3N[23] and Cu_3N[24] as sodium battery negative electrodes, which deliver lower capacities of ~100 mA h g^{-1} but provide better stable cycling behaviour compared with many other sodium battery negative electrode materials.[25] Mn_3N_2 films prepared by magnetron sputtering with a thickness of ~350 nm have recently been reported to exhibit capacities of up to 579 mA h g^{-1} in the 0-2.5 V range (*vs* Li) in lithium half cells, and retained 463 mA h g^{-1} of this capacity on the 110th cycle.[26] This material has not previously been examined *vs* lithium in more conventional composite electrodes, or *vs* sodium. MnO_2 and other manganese oxides are common positive electrode materials in primary and Li-ion batteries, taking advantage of their low cost and toxicity, high capacities and in some cases high potentials.[27]

Nitridation of manganese powder with ammonia at 600 °C yields Mn_2N,[28] whereas nanocrystalline Mn_4N and Mn_2N may be prepared by mechanical alloying and nitridation of Mn powders[29] and Mn_3N_2 has been produced by using NaN_3 to develop nitrogen pressure in an autoclave and nitriding manganese powder at 750 °C.[7] MnN was first prepared as a single phase by DC reactive sputtering in an Ar-N_2 mixture.[6] Mn_4N has been obtained from the solid state metathesis reactions of $MnCl_2$ with NaN_3[30] or Ca_3N_2,[31] and from MnI_2 with Li_3N,[32] and similar exchange reactions have been used to make crystals of Mn_6N_5 and Mn_3N_2 from MnI_2 and $NaNH_2$ in ammonia at 6 KBar and 400 to 600 °C.[33] Mn_3N_2 has also been prepared by solid state reaction of $MnCl_2$ with $LiNH_2$ followed by pyrolysis of the product in ammonia.[34] We have a long-standing interest in producing metal nitrides using solvothermal reactions using reactions of metal halides with ammonia or lithium amide,[35,36] including to make a variety of nanorod and nanotube structures. An important aspect of these reactions is that heat absorption by the solvent can be effective in targeting small crystallite materials. Hence we were interested in applying these methods to the manganese nitride system. The one previous solvothermal study of manganese nitride synthesis used NaN_3 as the nitrogen source and required temperatures to be raised extremely slowly to avoid self-propagating reactions.[37] $MnCl_2$ and NaN_3 were ground together and heated in toluene to 290 °C over a period of 3 days, then maintained for a further 3 days. This reaction produced MnN with stirred powders or a mixture of Mn_3N_2 and Mn_4N in the solid mixture was pelletised, presumably due to higher temperatures inside the pellets.

In our current study we report synthesis of nanocrystalline Mn_3N_2 through a solvothermal reaction between $MnCl_2$ and $LiNH_2$. We also assess its capability as an electrode material for aqueous supercapacitor applications, and as a negative electrode for sodium and lithium batteries.

Experimental

All procedures were carried out under nitrogen in glove box or Schlenk apparatus. Solvothermal synthesis was carried out in a 75 cm^3 Inconel autoclave (Parr 4740CH) with silica liner and a pressure gauge arm. Typically $MnCl_2$ (0.5 g, 4.0 mmol, Sigma-Aldrich) and $LiNH_2$ (0.19 g, 8 mmol, prepared from ^{n}BuLi and ammonia as described previously[36]) were ground together and placed in the autoclave liner. Benzene (20 cm^3, Fisher, dried by distillation from sodium) was added to the mixture and stirred with a spatula. The liner was sealed into the autoclave, which was heated at 350, 400,

450, 500 or 550 °C for 15 h and then allowed to cool to room temperature. No pressure was registered in the autoclave during these reactions. The black sample and the solvent were transferred to a Schlenk tube and filtered, then the solid was washed with 3 × 20 cm^3 methanol (Fisher, distilled from sodium methoxide) to remove lithium salts. The black product (~0.2 g) was dried *in vacuo* and collected inside the glove box under nitrogen.

Thermogravimetric analyses (TGA) used a Mettler Toledo TGA/SDTA85le, samples were heated at 10 °C min^{-1} to 900 °C under flowing Ar at 65 cm^3 min^{-1}. Powder X-ray diffraction (PXD) patterns were collected in Bragg-Brentano geometry using a Siemens D5000 (Cu-K$_{\alpha1}$) and a sealed sample holder. Rietveld refinements used the GSAS[38] package with standard structures taken from the ICSD[39] database. Crystallite sizes were extracted from the Lorentzian peak broadening using the method described in the GSAS manual[40] and a silica standard to fix the Gaussian instrumental peak shape terms. Transmission electron microscopy (TEM) data were collected with a Hitachi H7000 (75 kV) or a Jeol JEM3010 (300 kV), with samples prepared by ultrasound dispersion into dry toluene and dropping onto carbon-coated Cu grids. Combustion analysis (C, H and N) was outsourced to Medac Ltd and a WO$_3$ oxidant was added to aid combustion. Infrared spectroscopy was performed using CsI disks on a Perkin Elmer Spectrum One FT-IR spectrometer. Raman spectra were collected on Renishaw 2000 microscope in the frequency range of 2000 to 400 cm^{-1}, using He-Ne laser beam, 2.7 mW (power) with a wave length of 632.8 nm.

Electrochemical testing used a Biologic SP150 or MPG potentiostat. Working electrodes were made by depositing an ink of the active material onto 50 μm titanium (aqueous measurements, Advent research materials, 1.5 × 2.5 cm pieces, 1.5 × 1.5 cm area coated) or 5 μm copper (Advent research materials, 1 cm disks) foil substrates. The composite inks were produced in air from manganese nitride (75 wt%), acetylene black (20 wt%, Shawinigan, Chevron Phillips Chemical Co) and polyvinylidene fluoride (PVDF, Sigma-Aldrich, 5 wt%). PVDF was dissolved in cyclopentanone (Sigma-Aldrich, 1.5 cm^3 per 100 mg of composite) with 2 h stirring, then a ground mixture of Mn$_3$N$_2$ and acetylene black was added and the mixture stirred overnight. After dropping the ink onto the foil and allowing to dry, it was further dried overnight under vacuum at 120 °C, and the amount of active material on an electrode (~1.6 mg) was calculated by mass difference.

Aqueous electrochemical experiments used three electrode cells with a Hg/HgO reference electrode filled with 1 mol dm^{-3} aqueous KOH and a high surface area platinum gauze counter electrode. Electrochemical cells were assembled with 20 cm^3 of 1 mol dm^{-3} KOH$_{(aq)}$ electrolyte, which was degassed by bubbling nitrogen for 1 h through the solution then maintained as oxygen-free by passing nitrogen through the cell. The working electrode was then immersed and cyclic voltammograms (CVs) collected at various scan rates. Specific capacitance was calculated as half the integral of the CV trace / (scan rate × width of the potential window × mass of manganese nitride).

The lithium- and sodium-battery performance was tested in two-electrode Swagelok cells. Lithium cells were prepared with lithium metal foil (Sigma-Aldrich) as the counter and *pseudo* reference electrode, and a separator consisting of two sheets of dried Whatman GF/D borosilicate glass fibre soaked in 6 drops of a commercial 1 mol dm^{-3} LiPF$_6$ in ethylene carbonate/dimethyl carbonate (1:1) electrolyte (BASF). Sodium cells were assembled similarly using sodium metal foil (Sigma-Aldrich) and a 1 mol dm^{-3} NaPF$_6$ in ethylene carbonate/diethyl carbonate (1:1) electrolyte. The latter electrolyte components were purified separately (solvents distilled from BaO and NaPF$_6$ dried *in*

vacuo at 120 °C) before combining in the glove box. These cells were used to collect cyclic voltammograms or for galvanostatic cycling.

Results and Discussion

Reactions of $MnCl_2$ and $LiNH_2$ in benzene were carried out at various temperatures, and PXD patterns showed Mn_3N_2 through the reaction temperature range 350-550 °C, Fig. 1. Methanol washing was effective at removal of the lithium chloride by-product and the products contain no other crystalline impurities, apart from some Mn_2N due to thermal decomposition of the Mn_3N_2 at 550 °C. Rietveld fitting of these patterns yielded good fits and lattice parameters close to the literature values for Mn_3N_2, Table 1. Refinement of the Mn_2N phase fraction of the sample prepared at 550 °C showed it to be present at 10.4 wt%.
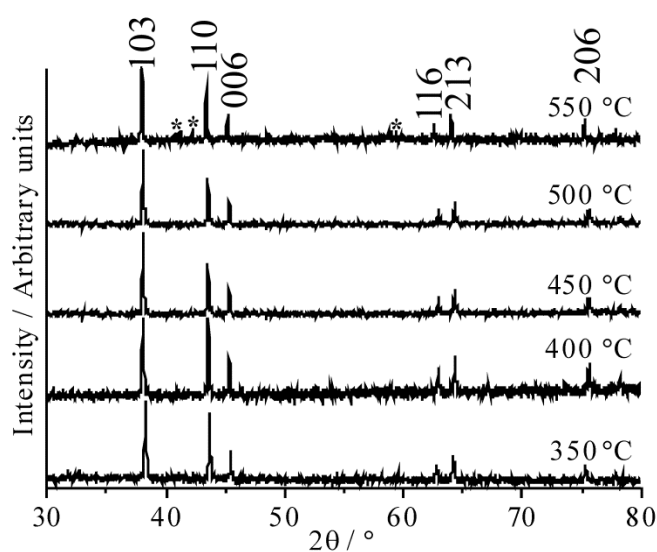

Fig. 1 PXD patterns of Mn_3N_2 samples prepared under solvothermal conditions at various temperatures. Reflections due to Mn_3N_2 are labelled with Miller indices and those due to Mn_2N at 550 °C labelled with asterisks.

Table 1 Rietveld fit parameters and compositions calculated from combustion analysis results for Mn_3N_2 samples prepared by solvothermal synthesis then washed with methanol.

Temperature / °C	Phase	a (Å)	b(Å)	c(Å)	R_{wp}, R_p / %	Crystallite size / nm	Analysed composition
350	Mn_3N_2	2.9733(3)		12.1258(12)	4.6 , 3.6	71	$MnN_{0.48}C_{0.02}H_{0.90}$
400	Mn_3N_2	2.977(3)		12.1422(14)	7.2 , 5.7	53	$MnN_{0.48}C_{0.02}H_{0.84}$
450	Mn_3N_2	2.977(2)		12.1417(10)	5.4 , 4.7	80	$MnN_{0.48}C_{0.02}H_{0.83}$
500	Mn_3N_2	2.9754(14)		12.1341(7)	4.8 , 3.8	75	$MnN_{0.43}C_{0.04}H_{0.86}$
550	Mn_3N_2	2.9728(4)		12.1238(6)	6.6 , 5.2	87	$MnN_{0.33}C_{0.32}H_{1.08}$
	Mn_2N	5.6609(2)	5.0574(4)	4.4449(7)		68	

η-Mn_3N_2 model in *I4/mmm* from Hasegawa and Yagi,[5] who reported a = 2.994(1) and c = 12.499(5) Å. ζ-Mn_2N in *Pbna* from Mekata *et al*,[28] who reported a = 5.668, b = 4.909 and c = 4.537 Å.

The solvothermal reaction of $MnCl_2$ with $LiNH_2$ presumably proceeds by metathesis reactions that substitute amide groups onto the manganese centres then condense with neighbouring manganese centres to yield nitride groups:

$$MnCl_2 + 2LiNH_2 \rightarrow \text{"}Mn(NH_2)_2\text{"} + 2LiCl$$

$$3\text{"}Mn(NH_2)_2\text{"} \rightarrow Mn_3N_2 + 4NH_3$$
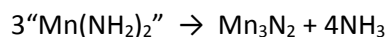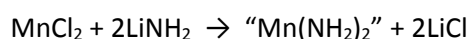
These are unlikely to proceed in two distinct steps as shown, and amide groups are likely to condense as they form. Note that the manganese oxidation state is retained – often in ammonolysis reactions of amides the first product during pyrolysis retains the starting oxidation state, and when $[Mn(N(SiMe_3)_2)_2]$ is reacted with ammonia a plateau in the TGA trace corresponding to manganese(II) was observed prior to nitrogen loss and crystallisation of Mn_4N.[41] The advantage of solvothermal conditions is that the crystallisation step often occurs at lower temperature.

Combustion analysis, Table 1, showed nitrogen to be present in the range 7.93-10.80 wt%, compared with a theoretical percentage of nitrogen in stoichiometric Mn_3N_2 of 14.5%. Hence all of these samples are nitrogen deficient. All samples contained carbon, with larger quantities found at the top of the synthesis temperature range where solvent decomposition was expected to be most significant.[36] Hydrogen was also found throughout, presumably due to some unreacted amide or imide groups. This was confirmed by IR spectra showing a broad $\nu(NH)$ peak at 3480-3490 cm^{-1} and a weaker $\delta(NH_2)$ at 1650-1700 cm^{-1},[42] as well as a weak $\nu(C-H)$ at 2890 to 2980 cm^{-1}. Nitrogen adsorption surface area measurements showed a gradual decrease in surface area, from 45 m^2 g^{-1} at 350 °C to 47, 33, 32 and 14 m^2 g^{-1} at 400, 450, 500 and 550 °C respectively. Samples prepared between 350 and 500 °C showed type IV isotherms with narrow hysteresis loops, with most of their pore volume concentrated into a single peak centred at ~3.3-3.8 nm. At 550 °C this distribution became much broader, with pore volume mainly observed over the size range 2-7 nm.

TEM showed an increasing degree of aggregation as the synthesis temperature was raised, Fig. 2, but also an interesting hollow capsule morphology in samples prepared at 350 °C, with lengths of 20-120 nm and ~20 nm diameter. Higher resolution images of the material obtained at 350 °C confirmed the hollow structures and showed that they are sometimes linked, and a selected area electron diffraction pattern of a region containing only this type of structure showed rings corresponding to the major diffraction peaks of Mn_3N_2. These are broad due to overlap between more than one reflection and not all reflections are observed, presumably reflecting the partial alignment of the particles that are lying flat on the TEM grid. Occasional particles of turbostratic carbon were also observed and high resolution TEM showed fringes with a spacing consistent with a graphitic structure.
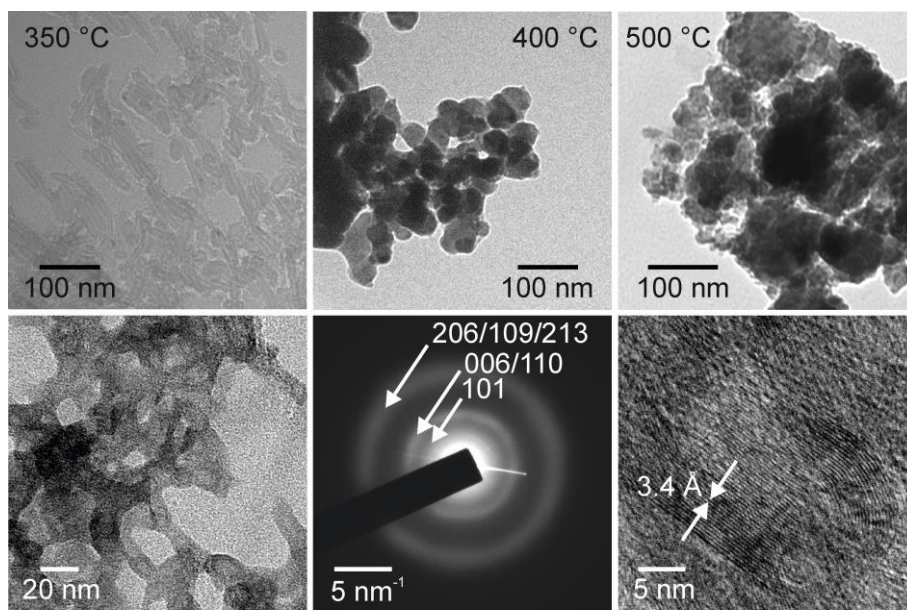
Fig. 2 TEM images of Mn₃N₂ samples made at various temperatures as labelled (top), and higher resolution images and electron diffraction of a sample made at 350 °C (bottom) showing Mn₃N₂ capsule structures (left), the selected area electron diffraction pattern of those capsules (middle) and lattice fringes from a carbon particle found in the sample (right).

Despite the low analysed carbon content the observation of graphitic structures in the TEM images of the samples prepared at 350 °C led to concerns about whether the capsule structures could be carbon-based, so Raman spectra were collected on samples prepared in the same way as those used for TEM. Specifically a suspension of the sample was prepared by ultrasonication, two drops ware placed on a TEM grid, then several drops of the same suspension on a glass microscope slide, then a final drop onto another TEM grid. The TEM grids were used to confirm that the sample morphology was consistent with other TEM samples. Once dry the sample on the glass slide was used to collect a Raman spectrum in the frequency range 2000-400 cm⁻¹ at several different locations. A strong single peak was observed at ~650 cm⁻¹, consistent with Mn-N and in a similar location to that observed in TiN, MoN and VN.[43] The peak was broad at 350 °C, became sharper at 400 °C and then grew in intensity as the crystallite size increased (Fig. 3). No Raman features associated with graphitic carbon were observed at ~1350 (D band) or ~1580 cm⁻¹ (G band).[44]
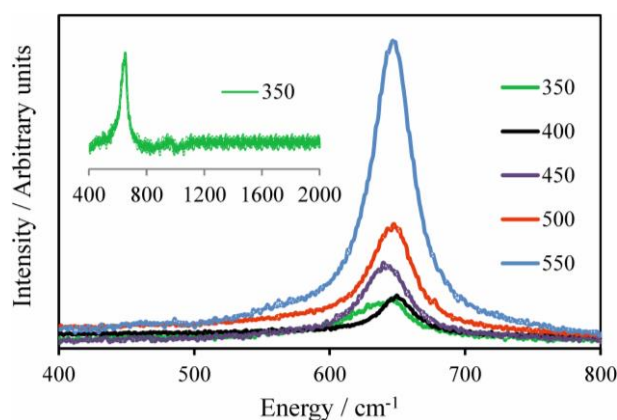

Fig. 3 Raman spectra of Mn₃N₂ synthesised at temperatures as labelled.

Aqueous electrochemistry (supercapacitor performance)

Metal nitrides have been tested as supercapacitor materials in various aqueous electrolytes including sulphuric acid or sodium sulphate solutions with molybdenum nitrides[12] and potassium hydroxide solutions with TiN or VN.[10,11] Mn_3N_2 was found to be highly unstable in acidic electrolytes so testing focussed on the electrochemistry in KOH solution. Titanium foils were used as the current collector as the foils themselves had very low capacitance (~0.1 F) and did not develop any new features on extended cycling in the electrolytes used. Cyclic voltammograms were collected in a potential window of -0.6 to +0.3 V vs Hg/HgO, beyond which limits continuously increasing reduction or oxidation features (respectively) were observed. With an uncoated titanium foil these features were observed at around -0.7 and +0.4 V, so the active material has a potential window only a little smaller than the solvent window.

Cyclic voltammograms (Fig. 4) were collected at various scan rates in 1 mol dm^{-3} aqueous KOH solution. In all cases changes to the shape of the CV curves were observed over the first few cycles and their areas (charge passed, which is proportional to the capacitance) were reduced as a result of these changes. This effect was least prominent in samples prepared at higher temperatures, and samples prepared at 550 °C showed only a small loss of area with cycling. The CV curves contained a number of oxidation and reduction peaks – at 100 mV s^{-1} scan rate only one reduction peak at around -0.15 V could be clearly distinguished in most samples, with a further peak at -0.40 V observable in samples prepared at 350 °C. This latter sample also more clearly exhibits multiple oxidation features, with peaks at -0.2 and 0.1 V, the 0.1 V peak appearing from its shape to be split and hence due to two process. At lower scan rates the presence of multiple oxidation and reduction processes becomes more obvious, with two main oxidation and reduction processes visible in each CV. These features are present in the first cycle, when the potential was first swept positive from the open circuit value of -0.32 V, suggesting that Mn^{2+} in Mn_3N_2 is oxidised to Mn^{4+} and reduced back to Mn^{2+}. A previous study of MnO_2 in $(NH_4)_2SO_{4(aq)}$ electrolyte showed CVs with no obvious peaks.[45]
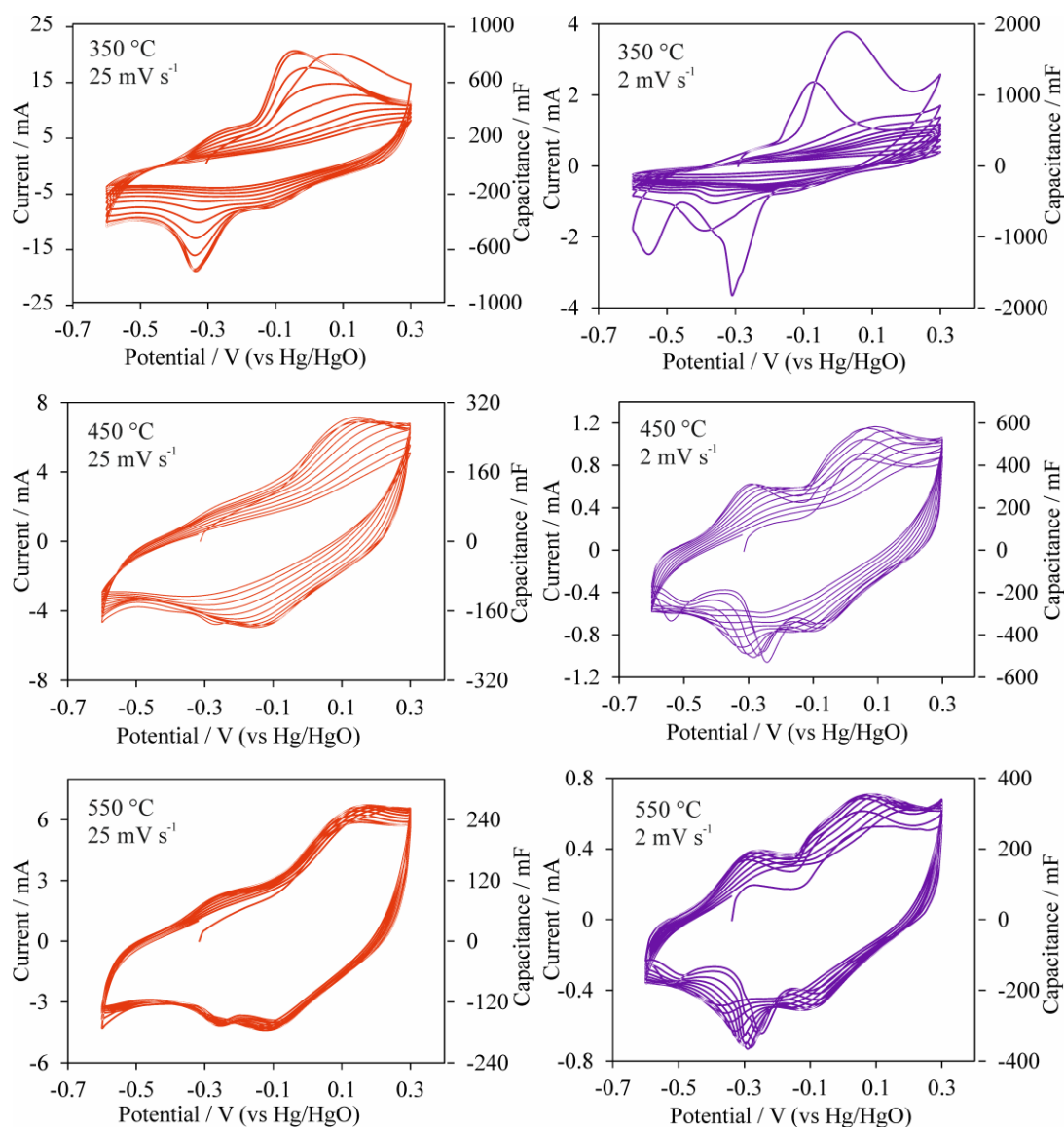
Fig. 4 CVs of manganese nitride samples produced at 350, 450 and 550 °C, with scan rates of 25 or 2 mV s^{-1}.

Capacitance can be calculated from the CV curves by dividing the charge passed by (2 × scan rate × potential window). The factor of 2 takes account of charging in both the positive and the negative direction in the curve. Variations in the capacitance for all samples and scan rates are shown in Fig. 5. Mn_3N_2 samples obtained at 350 °C show the highest first cycle capacitances of 299 F g^{-1} at 2 mV s^{-1}, or 130 F g^{-1} at 100 mV s^{-1}. However this capacitance is observed to steadily reduce during cycling, reaching values of 91 F g^{-1} at 2 mV s^{-1} or 98 F g^{-1} at 100 mV s^{-1} after just 10 cycles. After 10 cycles the curves are flattened out and redox peaks are of small magnitude, suggesting that chemical changes at the surface of the particles are reducing the redox activity and that double layer formation, rather than redox processes, is becoming responsible for the bulk of the capacitance. The larger drop at slow rates can be attributed to the length of time in each cycle that the electrode spends under oxidising or reducing conditions (whichever is causing damage). Increasing the annealing temperature results in samples with lower capacitances due to the lower surface areas, and similar losses on cycling (Fig. 5). The exception is that at the highest synthesis temperature studied (550 °C), although the capacitances were lower in the first cycle (123 F g^{-1} at 2 mV s^{-1} or 66 F g^{-1} at 100 mV s^{-1})

the drop in capacitance was proportionately less (118 F g^{-1} at 2 mV s^{-1} or 64 F g^{-1} at 100 mV s^{-1} in the 10th cycle).
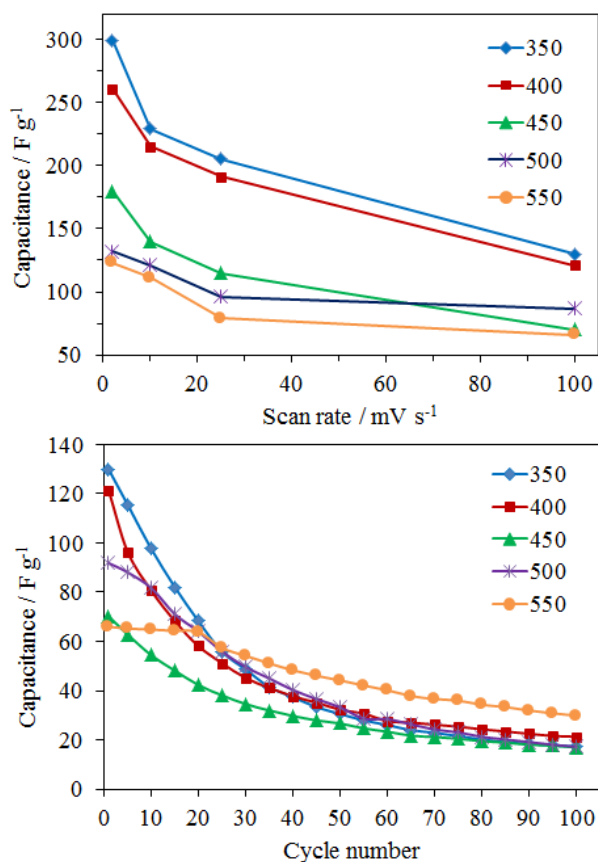

Fig. 5 Variation of first cycle specific capacitance of Mn$_3$N$_2$ samples with scan rate and annealing temperature (top) and variation with cycle number when scanned at 100 mV s^{-1} (bottom).

Electrochemistry in lithium and sodium electrolytes (battery performance)

Our previous work using conversion reactions of metal nitrides in sodium cells has shown that performance is intimately linked with surface area, hence these studies focussed on samples produced at 350 °C. A previous report shows thin Mn$_3$N$_2$ films cycled vs lithium in a Li$^+$-containing electrolyte to have a reversible capacity of 500 mA h g^{-1} or more, depending on the current, and good cycling capability.[26] Hence initially our composite electrodes containing nanocrystalline Mn$_3$N$_2$ were tested in lithium cells with a 1 mol dm^{-3} LiPF$_6$ in EC/DMC electrolyte.

CVs of lithium half cells (Fig. 6) showed reduction features at 0.7 and ~0 V vs Li in the first cycle, with the 0.7 V feature moving to ~0.9 V in subsequent cycles and gradually losing intensity. Oxidation features were observed at 0.5 and 1.3 V. Two features were also observed at slightly different potentials in thin films[26] and support the assumption that Mn$_3$N$_2$ is being reduced to manganese metal during cycling. Galvanostatic cycling at 200 mA g^{-1} (equivalent to 0.24C based on reduction to Mn and Li$_3$N with a theoretical capacity of 833 mA h g^{-1}) resulted in multiple features and a larger than theoretical capacity during the first reduction, suggesting other processes including solid electrolyte interface (SEI) formation during this step, but then two oxidation features. The capacity then settled into high reversible values of around 600 mA h g^{-1} in the initial cycles, similar to that

observed in thin films,[26] but gradually reduced until the capacity was 340 mA h g^{-1} after 50 cycles. During reduction almost all charge is passed in the potential region below 2 V, but during oxidation (which is the discharge process in the context of a lithium-ion cell) the proportion of the charge passed in the potential region 0.001-2 V is around 57% in the first cycle, improving to 97% in the 50th.
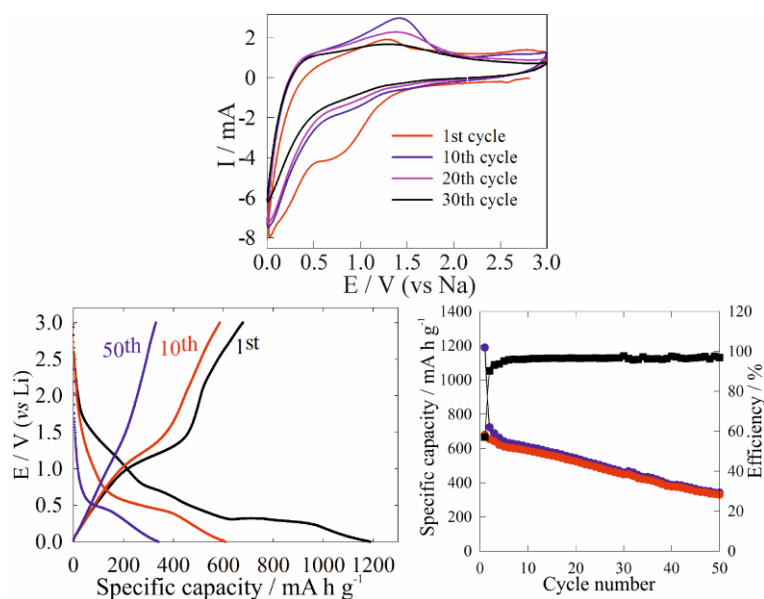

Fig. 6 CV (10 mV s^{-1}) in a lithium half cell (1M LiPF$_6$ in EC/DMC electrolyte), of an electrode prepared with Mn$_3$N$_2$ made at 350 °C (top), voltage profile during galvanostatic reduction and oxidation at 200 mA g^{-1} (bottom left) and specific capacity vs cycle number at 200 mA g^{-1} (bottom right). In the latter plot reduction capacity is marked in blue, oxidation capacity in red and Coulombic efficiency in black.

The lower current level of development level in sodium battery negative electrodes compared with those for lithium cells[25] makes new materials particularly interesting in this application. The CV in a sodium half cell showed multiple reduction features in the first cycle, but a much simpler oxidation profile and simple reduction profiles in all subsequent cycles. Galvanostatic reduction at 200 mA g^{-1} (0.24C) showed a first cycle reduction capacity of 486 mA h g^{-1} with multiple features in the potential trace, and as with lithium the first cycle oxidation capacity (1189 mA h g^{-1}), and subsequent reduction and oxidation capacities (87 and 81 mA h g^{-1} respectively in the 10th cycle, and 78 and 77 mA h g^{-1} in the 50th), were smaller. Notably the cycling behaviour is good, only 33% of the reduction capacity and 9% of the oxidation capacity is lost between the 2nd and 50th cycle. During reduction virtually all the charge is passed in the potential region below 2 V, whereas during oxidation 68% is passed below 2 V (based on the 50th cycle). Reducing the current to 50 mA g^{-1} (0.06C) a larger first reduction capacity of 623 mA h g^{-1} was observed, with 156 mA h g^{-1} recovered in the first oxidation. The higher values also persisted during cycling, which again showed good stability, e.g. the reduction capacity was 142 mA h g^{-1} in the 10th cycle and 127 mA h g^{-1} in the 50th cycle.
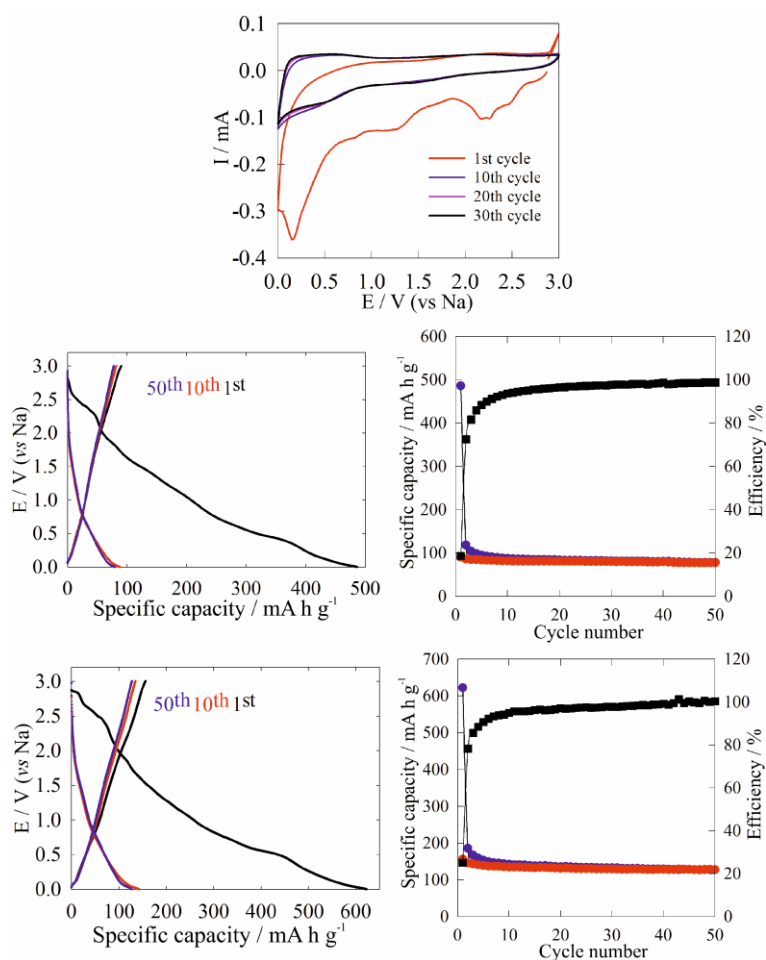
Fig. 7 CV (10 mV s^{-1}) in a sodium half cell (1M NaPF$_6$ in EC/DEC) of an electrode prepared with Mn$_3$N$_2$ made at 350 °C (top), and voltage profile during galvanostatic reduction and oxidation (left) and specific capacity vs cycle number (right) at 200 mA g^{-1} (centre) and 50 mA g^{-1} (bottom). In the capacity vs cycle number plots reduction capacity is marked in blue, oxidation capacity in red and Coulombic efficiency in black.

Conclusions

Solvothermal synthesis from MnCl$_2$ and LiNH$_2$ is an effective route to make nanocrystalline Mn$_3$N$_2$, with unusual nanocapsule morphologies at 350 °C synthesis temperature giving way to loose aggregates of nanoparticles at higher temperature until at 550 °C some decomposition to Mn$_2$N is introduced. These particles can store charge in aqueous potassium hydroxide solutions with capacities observed over 100 F g^{-1} at low scan rates, but were subject to significant capacity fade on cycling. In lithium half cells good initial capacities were observed but these were also subject to fading during cycling. Performance in sodium half cells was much more competitive, although this is partly due to the lower general development level in these systems. At charge/discharge rates equivalent to 6% of the theoretical capacity per hour based on reduction to manganese metal, good cycling behaviour, high Coulombic efficiency and 127 mA h g^{-1} capacity after 50 cycles were observed in such cells.

11

Acknowledgements

References

[1] C. Guillaud and J. Wyart, *Rev. Metall.*, 1948, **45**, 271-276.

[2] A. Leineweber, H. Jacobs and W. Kockelmann, *J. Alloys Cmpds.*, 2004, **368**, 229-247.

[3] M. Aoki, H. Yamane, M. Shimada and T. Kajiwara, *Mater. Res. Bull.*, 2004, **39**, 827-832.

[4] G. Kreiner and H. Jacobs, *J. Alloys Cmpds.*, 1992, **183**, 345-362.

[5] M. Hasegawa and T. Yagi, *J. Alloys Cmpds.*, 2005, **403**, 131-142.

[6] K. Suzuki, T. Kaneko, H. Yoshida, Y. Obi, H. Fujimori and H. Morita, *J. Alloys Cmpds.*, 2000, **306**, 66-71.

[7] A. Leineweber, R. Niewa, H. Jacobs and W. Kockelmann, *J. Mater. Chem.*, 2000, **10**, 2827-2834.

[8] W. J. Takei, R. R. Heikes and G. Shirane, *Phys. Rev.*, 1962, **125**, 1893-1897.

[9] S. Dong, X. Chen, X. Zhang and G. Cui, *Coord. Chem. Rev.*, 2013, **257**, 1946-1956.

[10] R. A. Janes, M. Aldissi and R. B. Kaner, *Chem. Mater.*, 2003, **15**, 4431-4435.

[11] D. Choi, G. E. Blomgren and P. N. Kumta, *Adv. Mater.*, 2006, **18**, 1178-1182.

[12] S. I. U. Shah, A. L. Hector and J. R. Owen, *J. Power Sources*, 2014, **266**, 456-463.

[13] D. Yang, *Application of nanocomposites for supercapacitors: characteristics and properties*, chapter 12 in *Nanocomposites - new trends and developments*, F. Ebrahimi (Ed), Intech, 2012 (DOI:10.5772/50409).

[14] M. Toupin, T. Brousse and D. Bélanger, *Chem. Mater.*, 2004, **16**, 3184-3190.

[15] A. J. Roberts and R. C. T. Slade, *J. Mater. Chem.*, 2010, **20**, 3221-3226.

[16] J.Cabana, L. Monconduit, D. Larcher and M. R. Palacín, *Adv. Mater.*, 2010, **22**, E170-E192.

[17] Z. W. Fu, Y. Wang, X. L. Yue, S. L. Zhao and Q. Z. Qin, *J. Phys. Chem. B*, 2004, **108**, 2236-2244; Q. Sun and Z. W. Fu, *Electrochem. Sol. St. Lett.*, 2007, **10**, A189-A193; Q. Sun and Z. W. Fu, *Electrochem. Sol. St. Lett.*, 2008, **11**, A233-A237; Q. Sun, Z. W. Fu, *Electrochim. Acta*, 2008, **54**, 403-409.

[18] Y. Wang, W. Y. Liu and Z. W. Fu, *Acta Phys. Chim. Sin.*, 2006, **22**, 65-70.

[19] Y. Wang, Z. W. Fu, X. L. Yue and Q. Z. Qin, *J. Electrochem. Soc.*, 2004, **151**, E162-E167.

[20] B. Das, M. V. Reddy, P. Malar, T. Osipowicz, G. V. S. Rao and B. V. R. Chowdari, *Sol. St. Ionics*, 2009, **180**, 1061-1068.

[21] F. Gillot, J. Oro-Sole and M. R. Palacín, *J. Mater. Chem.*, 2011, **21**, 9997-10002.

[22] J. Ma, L. Yu and Z. W. Fu, *Electrochim. Acta*, 2006, **51**, 4802-4814; N. Pereira, L. Dupont, J. M. Tarascon, L. C. Klein and G. G. Amatucci, *J. Electrochem. Soc.,* 2003, **159**, A1273-A1280.

[23] X. Li, M. M. Hasan, A. L. Hector and J. R. Owen, *J. Mater. Chem. A*, 2013, **1**, 6441-6445.

[24] X. Li, A. L. Hector and J. R. Owen, *J. Phys. Chem. C*, in press (DOI:10.1021/jp509385w).

[25] V. Palomares, P. Serras, I. Villaluenga, K. B. Hueso, J. Carretero-González and T. Rojo, *Energy Environ. Sci.*, 2012, **5**, 5884-5901.

[26] Q. Sun and Z.-W. Fu, *Appl. Surf. Sci.*, 2012, **258**, 3197-3201.

[27] K. Zhang, X. Han, Z. Hu, X. Zhang, Z. Tao and J. Chen, *Chem. Soc. Rev.*, in press (DOI:10.1039/c4cs00218k).

[28] M. Mekata, J. Haruna and H. Takaki, *J. Phys. Soc. Jpn.*, 1968, **25**, 234-238.

[29] W. J. Feng, N. K. Sun, J. Du, Q. Zhang, X. G. Liu, Y. F. Deng and Z. D. Zhang, *Sol. St. Commun.*, 2008, **148**, 199-202.

[30] A. L. Hector and I. P. Parkin, *Polyhedron*, 1995, **14**, 913-917.

[31] A. L. Hector and I. P. Parkin, *Chem. Mater.*, 1996, **7**, 1728-1733.

[32] J. C. Fitzmaurice, A. L. Hector and I. P. Parkin, *J. Chem. Soc., Dalton Trans.*, 1993, 2435-2438.

[33] G. Kreiner and H. Jacobs, *J. Alloys Cmpds.*, 1992, **183**, 345-362.

[34] I. P. Parkin and A. T. Rowley, *J. Mater. Chem.*, 1995, **5**, 909-912.

[35] P. Chirico, A. L. Hector and B. Mazumder, *Dalton Trans.*, 2010, **39**, 6092-6097; B. Mazumder and A. L. Hector, *J. Mater. Chem.*, 2008, **18**, 1392-1398; P. Chirico and A. L. Hector, *Z. Naturforsch.*, 2010, **65b**, 1051-1057.

[36] B. Mazumder, P. Chirico and A. L. Hector, *Inorg. Chem.*, 2008, **47**, 9684-9690.

[37] J. Choi and E. G. Gillan, *Inorg. Chem.*, 2009, **48**, 4470-4477.

[38] A. C. Larson, R. B. Von Dreele, *Generalized Structure Analysis System (GSAS)*, Los Alamos National Laboratory Report LAUR (2004) 86-748; B. H. Toby, *J. Appl. Cryst.*, 2001, **34**, 210-213.

[39] Inorganic Crystal Structure Database (ICSD, Fiz Karlsruhe) accessed via the EPSRC-funded National Chemical Database Service hosted by the Royal Society of Chemistry.

[40] R. B. Von Dreele, A. C. Larson, GSAS manual, LANSCE MS-H805, Los Alamos National Laboratory, NM87545 (2000).

[41] D. V. Baxter, M. H. Chisholm, G. J. Gama, V. F. DiStasi, A. L. Hector and I. P. Parkin, *Chem. Mater.*, 1996, **8**, 1222-1228.

[42] K. Nakamoto, *Infrared and Raman Spectra of Inorganic and Organic Compounds*, 3rd ed.; J. Wiley, New York, 1978.

[43] O. Shebanova, E. Soignard and P. F. McMillan, *High Press. Res.*, 2006, **26**, 87-97.

[44] M. Fang, K. Wang, H. Lu, Y. Yang and S. Nutt, *J. Mater. Chem.*, 2009, **19**, 7098-7105; D. Yuan, X. Yuan, W. Zou, F. Zeng, X. Huang and X. Zhou, *J. Mater. Chem.*, 2012, **22**, 17820-17826.

[45] A. J. Roberts and R. C.T. Slade, *Electrochim. Acta*, 2010, **55**, 7460–7469.